

## AN ELECTROCHEMICAL STUDY OF H<sub>2</sub>O<sub>2</sub> DECOMPOSITION ON SINGLE-PHASE $\alpha$ -Fe<sub>2</sub>O<sub>3</sub> FILMS

Dong Fu

Department of Chemistry, The University of Western Ontario, 1151 Richmond St.,  
London, Ontario, Canada N6A 5B7

### ABSTRACT

The electrochemical kinetics of hydrogen peroxide on  $\alpha$ -Fe<sub>2</sub>O<sub>3</sub> films were studied over the pH range of 9.2 to 12.6 and the H<sub>2</sub>O<sub>2</sub> concentration range of 10<sup>-4</sup> to 10<sup>-2</sup> mol·dm<sup>-3</sup>. The Tafel slopes for H<sub>2</sub>O<sub>2</sub> reduction obtained from polarization measurements are 124 ± 6 independent of pH and the concentration of H<sub>2</sub>O<sub>2</sub>. H<sub>2</sub>O<sub>2</sub> oxidation reactions are adsorption behaviours, currents slightly increasing with potentials at lower overpotentials, and rapidly increasing with Tafel behaviours at higher overpotentials. Both the reduction and oxidation of H<sub>2</sub>O<sub>2</sub> on  $\alpha$ -Fe<sub>2</sub>O<sub>3</sub> have a first-order dependence on the concentration of molecular H<sub>2</sub>O<sub>2</sub>. However, for the pH dependence, the reduction has an inverse first-order dependence, whereas the oxidation has a first-order dependence, on the concentration of OH<sup>-</sup>. For both cases the electroactive species is the molecular H<sub>2</sub>O<sub>2</sub>, not its conjugate base form, HO<sub>2</sub><sup>-</sup>. Based on these observations, reaction kinetic mechanisms are proposed which involve adsorbed radical intermediates; HO•OH<sup>-</sup> and HO• for the reduction, and HO<sub>2</sub>•H<sup>+</sup>, HO<sub>2</sub>•, and •O<sub>2</sub><sup>-</sup> for the oxidation. These intermediates are assumed to be in linear adsorption equilibria with OH<sup>-</sup> and H<sup>+</sup> in the bulk aqueous phase, respectively, giving the observed pH dependences. The rate-determining step is the reduction or oxidation of the adsorbed H<sub>2</sub>O<sub>2</sub> to the corresponding intermediates, a reaction step which

involves the use of  $\text{Fe}^{\text{III}}/\text{Fe}^{\text{II}}$  sites in the  $\alpha\text{-Fe}_2\text{O}_3$  surface as an electron donor-acceptor relay. The rate constant for the  $\text{H}_2\text{O}_2$  decomposition on  $\alpha\text{-Fe}_2\text{O}_3$  determined from the oxidation and reduction Tafel lines is very low, indicating that the  $\alpha\text{-Fe}_2\text{O}_3$  surface is a poor catalyst for  $\text{H}_2\text{O}_2$  decomposition.

**Key Words:**  $\text{H}_2\text{O}_2$  decomposition, single-phase  $\gamma\text{-FeOOH}$  film, electrochemical oxidation and reduction, Tafel analysis

## 1.0 INTRODUCTION

The heat transport system (HTS) is one of important systems of a CANDU nuclear reactor. Inside the reactor core of HTS is consists of 2.5 wt% Nb alloy pressure tubes which connected to carbon steel pipes outside the core. Corrosion of these pipes under reactor operating conditions is a main concern for aging CANDU reactors.

For the assessment of various safety, operational and maintenance requirements for nuclear power plants, it is important to an accurate understanding of the effects of ionizing radiation on reactor system chemistry and steel corrosion. Of particular concern are the effects of the decomposition products of water radiolysis from ionizing radiation. Water decomposes to a range of redox species:  $\bullet\text{OH}$ ,  $\text{H}_2\text{O}_2$ ,  $\text{O}_2$ ,  $\text{H}_2$ ,  $\bullet\text{O}_2^-$ , etc under ionizing radiation conditions [1-3]. In a constant radiation field, corrosion behavior of steel are driven by the aqueous redox conditions which are determined by steady-state concentrations of these water decomposition products. The overall redox conditions are established by interactions between reactive radiolysis products, the steel surface and corrosion products produced by these reactions [3].  $\text{H}_2\text{O}_2$  is one of key products by radiation for the perspective of corrosion at ambient temperature [4-6].

However,  $\text{H}_2\text{O}_2$  consumption during corrosion and its surface-catalyzed decomposition can influence the concentrations of other radiolysis species by disturbing the steady-state balance between them [3].

The composition and structure/morphology of the oxide produced by corrosion on corrodible materials such as carbon steel will strongly influence the  $\text{H}_2\text{O}_2$  decomposition kinetics. The surface oxides formed on carbon steel under irradiation range from  $\text{Fe}_3\text{O}_4$  to  $\gamma\text{-Fe}_2\text{O}_3$  and  $\gamma\text{-FeOOH}$ , and/or complex mixtures of these oxides [4, 7], and vary considerably in reactivity and solubility, making the processes involved in assessing the corrosion chemistry of steel notoriously complex [8]. Among these oxides, hematite,  $\alpha\text{-Fe}_2\text{O}_3$ , is an important corrosion product of carbon steel at higher operation temperature ( $\sim 150^\circ\text{C}$ ) in HTS of nuclear reactor [9-10]. By studying the behaviour of  $\text{H}_2\text{O}_2$  on individual oxides/hydroxides we hope to be able to characterize the overall steel corrosion kinetics in the presence of ionizing radiation.

The kinetics of  $\text{H}_2\text{O}_2$  decomposition on the iron oxide surface strongly depends on a range of experimental conditions, such as pH,  $[\text{H}_2\text{O}_2]$ , and the morphology and composition of the surface. Although iron oxide surfaces are catalysts for the decomposition of  $\text{H}_2\text{O}_2$ , the mechanism is still not well established [11]. Some researchers report the decomposition of  $\text{H}_2\text{O}_2$  on various catalyst surfaces suggesting highly reactive intermediates involved [12-20]. On iron oxide surfaces, it is generally accepted that the catalytic decomposition of  $\text{H}_2\text{O}_2$  at low pH occurs by its reduction via the classical Fenton reaction [21]:



coupled with  $\text{H}_2\text{O}_2$  oxidation



These reactions occur primarily on the solid oxide surface, and concentrations of dissolved  $\text{Fe}^{2+}$  and  $\text{Fe}^{3+}$  species are very low. The decomposition rate of  $\text{H}_2\text{O}_2$  in the aqueous phase containing similar low levels of dissolved iron species in the absence of an iron oxide surface, is reported to be two orders of magnitude lower [22]. More recent researchers have proposed reaction mechanisms in modified forms, involving other intermediates such as  $\text{HO}_2\cdot$  and  $\cdot\text{O}_2^-$  in addition to the hydroxyl radical [20, 22-29]. Whether Fenton or Fenton-like reactions are still favorable at neutral to high pH is not known, since few studies at high pH have been reported [30].

The objective of this study is to establish the reaction mechanism and kinetic parameters for  $\text{H}_2\text{O}_2$  decomposition on  $\alpha\text{-Fe}_2\text{O}_3$  in near neutral to basic conditions, pH 9.2 – 12.6. The  $\text{H}_2\text{O}_2$  decomposition kinetics was studied by electrochemical measurements on a  $\alpha\text{-Fe}_2\text{O}_3$  film chemically deposited on indium tin oxide (ITO). Our overall aim is to determine how radiolytic oxidants, e.g.  $\text{H}_2\text{O}_2$ , will interact with oxide-covered steel surfaces, and how this interaction will influence the overall steel corrosion kinetics in the presence of ionizing radiation.

## 2.0 EXPERIMENTAL

The  $\alpha\text{-Fe}_2\text{O}_3$  films on ITO glass were prepared by a forced hydrolysis method reported previously [31]. Briefly, ITO glass slides (15 mm  $\times$  75 mm, Delta Technologies, Limited), were immersed in a  $2 \times 10^{-2}$  mol·dm<sup>-3</sup>  $\text{Fe}(\text{NO}_3)_3$  solution at 60°C for 12 h, allowing hydrolyzed  $\text{Fe}^{\text{III}}$  species to deposit on the ITO glasses. The electrode was then removed from the solution, rinsed with distilled water, and suspended in air to dry at ambient temperature for 24 h and then heated 2h at 400°C. The film deposition was performed in batches, and one of the samples from each batch was characterized by SEM, X-ray diffraction and Raman Spectroscopy to confirm that the films grown were single-phase  $\alpha\text{-Fe}_2\text{O}_3$ , as described in detail elsewhere [31]. The surface

morphology and the cross section of the film were examined by SEM and its chemical composition and phase structure were confirmed by Raman and XRD spectroscopy, Figure 1. The thickness of the films was typically ~100 nm.

A standard three-electrode cell was used for all experiments. The working electrode was the  $\alpha$ -Fe<sub>2</sub>O<sub>3</sub>/ITO glass electrode, and the surface area exposed to solution was controlled at 1.0 cm<sup>2</sup> by masking the excess surface area with silicon glue (3M™). The reference electrode was a saturated calomel electrode (SCE) and the counter electrode a platinum mesh. All potentials were measured, and are quoted, on the SCE scale. The supporting electrolyte was 0.1 mol·dm<sup>-3</sup> NaClO<sub>4</sub> (Fisher Scientific), to ensure solution conductivity, and contained 1 × 10<sup>-2</sup> mol·dm<sup>-3</sup> borate (Na<sub>2</sub>B<sub>4</sub>O<sub>7</sub>, Caledon Laboratories Ltd) to provide a good buffer capacity in the pH range studied, 9.2 – 12.6. The pH was adjusted by adding drops of 1 mol·dm<sup>-3</sup> NaOH or solid boric acid. A desired concentration of H<sub>2</sub>O<sub>2</sub>, in the range of 5 × 10<sup>-4</sup> – 1 × 10<sup>-2</sup> mol·dm<sup>-3</sup>, was achieved by adding an appropriate amount of H<sub>2</sub>O<sub>2</sub> stock solution (3% w/w, Fisher Scientific). All solutions were prepared with water purified using a NANOpure Diamond UV ultrapure water system (resistivity of 18.2 MΩ·cm).

In potentiodynamic experiments, performed as a function of H<sub>2</sub>O<sub>2</sub> concentration and pH, the current was monitored while the potential (E) was varied linearly at a sweep rate of 0.17 mV s<sup>-1</sup> from the open circuit potential, E<sub>OC</sub>, to either E<sub>OC</sub> + 0.4 V or E<sub>OC</sub> – 0.4 V. Each set of scans was conducted on a freshly prepared  $\alpha$ -Fe<sub>2</sub>O<sub>3</sub> film to minimize the influence of surface changes during the experiments. A Solartron model 1240 potentiostat was used in all electrochemical measurements. Corrware™ software (supplied by Scribner and Associates) was used to control experiments.

The X-ray diffraction analysis of the  $\alpha$ -Fe<sub>2</sub>O<sub>3</sub> films was carried out on a Rigaku RTP 300RC diffractometer (rate 10°/min, step 0.02°) using Co-K $\alpha$  radiation (45 kV, 160 mA, X-ray wavelength 1.790210Å ).

The Raman spectra of the  $\alpha$ -Fe<sub>2</sub>O<sub>3</sub>/ITO electrode surfaces were obtained using a Renishaw Ramascope Model 2000, using a 633 nm laser wavelength, at approximately 2 mW at the sample (100% power).

### 3.0 RESULTS AND DISCUSSION

#### 3.1 *Open Circuit Potential on $\alpha$ -Fe<sub>2</sub>O<sub>3</sub> in H<sub>2</sub>O<sub>2</sub> Solution*

For a given pH, the open circuit potential (E<sub>OC</sub>) recorded on the  $\alpha$ -Fe<sub>2</sub>O<sub>3</sub> film on ITO glass electrode was slightly increase with of H<sub>2</sub>O<sub>2</sub> concentration, Figure 2. Also shown in the figure are the calculated equilibrium potentials as a function of pH for the redox reactions possible on the  $\alpha$ -Fe<sub>2</sub>O<sub>3</sub> film:



The E<sub>OC</sub> values lie between the equilibrium potentials (E<sup>eq</sup>) for H<sub>2</sub>O<sub>2</sub> oxidation (reaction 3) and reduction (reaction 4) for all 4 H<sub>2</sub>O<sub>2</sub> concentrations and slightly above the equilibrium potential for the H<sub>2</sub>O<sub>2</sub>/O<sub>2</sub> redox couple (reaction 4). This makes it feasible for the surface to support the decomposition of H<sub>2</sub>O<sub>2</sub> via the coupling of reactions 3 and 4 to yield the overall reaction:



For coupled reactions, the proximity of the open circuit potential to the equilibrium potential of reaction 4 indicates that reaction 4 rate is much faster than reaction 3. The identical pH-

dependencies clearly indicate that the  $\text{H}_2\text{O}_2$  decomposition reaction mechanism and relational reaction rates of reaction 3 and 4 is not significantly changed.

According to Lin *et al* [22],  $\text{Fe}^{\text{III}}$  in high valence iron oxides can be reduced to  $\text{Fe}^{\text{II}}$  and  $\text{H}_2\text{O}_2$  oxidized to  $\text{HO}_2\cdot$  and with charge balance being maintained by  $\text{H}^+$ .  $\text{Fe}^{\text{II}}$  can be oxidized to  $\text{Fe}^{\text{III}}$  and  $\text{OH}^-$  (i.e. classic Fenton reaction, reaction 2). This process is reversible and does not lead to an irreversible phase transformation. Hence,  $\alpha\text{-Fe}_2\text{O}_3$  can be considered reversibly reducible over the range investigated, making the oxide a potential redox catalysts for  $\text{H}_2\text{O}_2$  decomposition. The stability of  $\alpha\text{-Fe}_2\text{O}_3$  in our experiments was examined by recording Raman Spectra before and after exposure of an electrode to a solution containing  $0.01 \text{ mol}\cdot\text{dm}^{-3}$  of  $\text{H}_2\text{O}_2$  for longer than 24 h. No change in the Raman spectra was observed. Although changes to a thin outer-layer of the deposit would be undetectable by Raman, making the results inconclusive, the open circuit potential lies above the equilibrium potentials of all of the iron oxide/hydroxide reactions, indicating that the electrochemical conversion of the hydroxide is not likely.

Band gap of  $\alpha\text{-Fe}_2\text{O}_3$  is 2.2 eV, determinates  $\alpha\text{-Fe}_2\text{O}_3$  is a semiconductor [32]. This would be sufficient to maintain conductivity between the anodic and cathodic sites thereby allowing the surface to act as a redox catalyst. A key observation is that  $E_{\text{OC}}$  is insignificantly dependent of  $[\text{H}_2\text{O}_2]$  for a given pH, indicating changes in  $[\text{H}_2\text{O}_2]$  should influence the equilibrium potentials of both reactions near equally, but with opposite shifts if  $\text{H}_2\text{O}_2$  decomposition was occurring. For this to be the case,  $\text{H}_2\text{O}_2$  should be in close to equilibrium with the surface and/or the kinetics of both reactions 3 and 4 have identical concentration dependencies.

### 3.2 *The Current-Potential Profile*

#### 3.2.1 $\text{H}_2\text{O}_2$ -free solutions

The currents recorded during potentiodynamic scans were recorded as a function of pH in H<sub>2</sub>O<sub>2</sub>-free Ar-purged solution to establish the baseline current-potential profiles, Figure 3. In these experiments, the potential was scanned from E<sub>OC</sub> to E<sub>OC</sub> + 0.4 V, and then reversed and scanned to typically E<sub>OC</sub> - 0.4 V, at a scan rate of 0.17 mV·s<sup>-1</sup>. At this scan rate, the currents observed during the forward and reverse scans differed only slightly. The difference, however, increased linearly with an increase in scan rate (results not shown), and is attributed to capacitance charging on the surface. In all cases, a very small cathodic current offset, approximately  $-1.5 \times 10^{-9}$  A·cm<sup>-2</sup>, was observed. This offset current is independent of scan rate. The value of this offset is very small and close to current resolution of the instruments. Therefore, the influence of the offset current was ignored from the measured currents in the Tafel analyses discussed in the following sections.

At a larger potential range -0.4 – +0.6 V, the current near constant except pH 12.6, which increases sharply at +0.55V due to water oxidation at lower potential at high pH. For lower negative polarization current is slightly increase probably due to the onset of  $\alpha$ -Fe<sub>2</sub>O<sub>3</sub> reduction to Fe<sub>3</sub>O<sub>4</sub> as claimed for thermodynamics favourable. The currents observed in the H<sub>2</sub>O<sub>2</sub>-free solutions are referred to as the baseline currents, hereafter. These currents were not considered from the measured currents in the Tafel analyses discussed below since the current is magnitude 10<sup>-2</sup> smaller compared to the currents eventually measured in H<sub>2</sub>O<sub>2</sub> solutions.

### 3.2.2 In H<sub>2</sub>O<sub>2</sub> solutions

Current-potential profiles were obtained as a function of [H<sub>2</sub>O<sub>2</sub>] and pH. The profiles observed as a function of [H<sub>2</sub>O<sub>2</sub>] at pH 10.6 are plotted in Fig. 4. The upper panels show the *log* *|j|* vs *E* plots obtained during cathodic (Fig. 4a) and anodic scans (Fig. 4b) without any baseline-current correction, while the lower panels show *log* *|j|* vs *E* plots corrected for the baseline

currents (Fig. 4c and 4d). The baseline currents are insignificant (1%) and all  $\log |j|$  vs  $E$  profiles presented hereafter are not baseline-corrected.

### 3.3 Cathodic Reduction of $H_2O_2$ on $\alpha-Fe_2O_3$

#### 3.3.1 The current-potential profile

Examples of the  $\log |j_c|$  vs  $E$  plots obtained are shown in Fig. 5. Fig. 5a shows the plots obtained at pH = 10.6 as a function of  $[H_2O_2]$  and Fig. 5b the plots obtained at  $[H_2O_2] = 1 \times 10^{-3}$  mol·dm<sup>-3</sup> as a function of pH. The  $\log |j_c|$  vs  $E$  plots exhibit well-defined Tafel regions over the potential range  $E_{OC}$  to  $(E_{OC} - 0.3 \text{ V})$  with a slope of  $124 \pm 6 \text{ mV} \cdot \text{dec}^{-1}$ , independent of  $[H_2O_2]$  and pH. These slopes are approaching the theoretical value of  $118 \text{ mV} \cdot \text{dec}^{-1}$  expected for a one-electron transfer rate-limiting reaction.

The plots at the two lowest pH values can be made to overlap if shifted by  $-59 \text{ mV}$  per  $\log [H_2O_2]$  and  $+59 \text{ mV}$  per pH unit. For the two higher pH values, overlap requires an additional shift of  $+11 \text{ mV}$  (pH = 11.5) and  $+54 \text{ mV}$  (pH = 12.6). These additional shifts account for the difference between the actual concentration of  $H_2O_2$  (designated as  $[^mH_2O_2]$ ) and the analytically-added value (designated as  $[H_2O_2]$ ). Based on a  $pK_a = 11.65$  for the  $H_2O_2$  dissociation reaction, the concentration adjustments are given by:

$$[^mH_2O_2] = 0.64 [H_2O_2] \text{ at pH} = 11.5 \quad (7a)$$

$$[^mH_2O_2] = 0.12 [H_2O_2] \text{ at pH} = 12.6 \quad (7b)$$

allowing the pH-dependence of the acid-base equilibrium to be eliminated. These adjusted plots, using the profile for  $1 \times 10^{-3}$  mol·dm<sup>-3</sup> and pH = 10.6 as the reference cases, are shown in Fig. 5c and 5d.

These results strongly suggest that the  $[^mH_2O_2]$  or pH dependence of the  $\log |j_c|$  vs  $E$  profiles arise from the  $[^mH_2O_2]$  or pH dependence of the equilibrium potential of the

decomposition reaction, and that changes in  $[{}^m\text{H}_2\text{O}_2]$  or pH do not change the rate-determining step. Fig. 5 also shows that the current-potential behaviour begins to deviate from the Tafel slope for a one-electron transfer process at more negative potentials (less than  $E_{\text{OC}} - 0.3 \text{ V}$ ). This is attributable to the onset of either diffusion control or reduction of  $\text{Fe}^{\text{III}}$  to  $\text{Fe}^{\text{II}}$ . At potentials above  $E_{\text{OC}} - 0.3 \text{ V}$ , the currents are sufficiently low that any influence of  $\text{H}_2\text{O}_2$  diffusion should be negligible. At more cathodic potentials diffusion may partially control the current when the charge transfer rate at the interface becomes large. The sharp increases in current due to the reduction of  $\text{Fe}^{\text{III}}$  to  $\text{Fe}^{\text{II}}$  observed in the  $\text{H}_2\text{O}_2$ -free solutions also occurs at more cathodic potentials (as discussed above). This region was avoided, and the Tafel analysis limited to the potential range from  $E_{\text{OC}}$  to  $E_{\text{OC}} - 0.3 \text{ V}$ .

### 3.3.2 Mechanism for Cathodic Reduction of $\text{H}_2\text{O}_2$ to $\text{OH}^-$ on $\alpha\text{-Fe}_2\text{O}_3$

A reaction kinetic mechanism consistent with these observations is shown in Fig. 6. The adsorption of a variety of molecular adsorbates on iron oxides/hydroxides have been shown to follow the Langmuir isotherm [32-33]. Thus, it is assumed that a rapid equilibration between aqueous (aq) and surface adsorbed (ad)  $\text{H}_2\text{O}_2$  is established



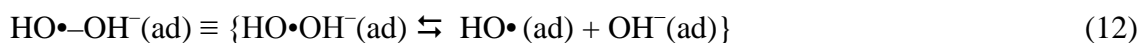
which for low to intermediate surface coverages can be assumed to obey a linear adsorption or Langmuir isotherm:

$$K_{\text{H}_2\text{O}_2}^{\text{ad}} \approx \frac{[{}^m\text{H}_2\text{O}_2(\text{ad})]}{[{}^m\text{H}_2\text{O}_2(\text{aq})]} \quad (10)$$

Subsequently, electron transfer to the adsorbed state occurs:



a process likely to involve a donor-acceptor electron relay between adjacent  $\text{Fe}^{\text{III}}/\text{Fe}^{\text{II}}$  states in the electrode surface. The adsorbed intermediate,  $\text{HO}\cdot\text{-OH}^{\text{-}}(\text{ad})$ , represents all reduced forms of  $\text{H}_2\text{O}_2$ , ranging from the hydrogen-peroxide anion radical,  $\text{HO}\cdot\text{OH}^{\text{-}}(\text{ad})$ , to the completely dissociated pair,  $\text{HO}\cdot(\text{ad})$  and  $\text{OH}^{\text{-}}(\text{ad})$ :



The formation of the intermediate radicals from the reactions of  $\text{H}_2\text{O}_2$  with dissolved iron species,  $\text{Fe}^{2+}$  and  $\text{Fe}^{3+}$ , is well established, and, in particular, the reaction of  $\text{H}_2\text{O}_2$  with  $\text{Fe}^{2+}$  forming  $\cdot\text{OH} + \text{OH}^{\text{-}} + \text{Fe}^{3+}$  is the well known Fenton reaction [21, 33]. Although one could argue whether the same reactions occur on oxide or hydroxide surfaces, it is not an unreasonable assumption, and has been invoked by others [15-16, 30].

These radical intermediate surface species are able to desorb, and therefore, assumed to be in adsorption-desorption equilibrium:



$$\left(K_{red}^{ad}\right)' = \frac{[\text{HO}\cdot\text{-OH}^{\text{-}}(\text{aq})]}{[\text{HO}\cdot\text{-OH}^{\text{-}}(\text{ad})]} \quad (14)$$

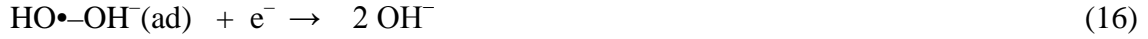
where  $\left(K_{red}^{ad}\right)'$  is the adsorbed-aqueous phase equilibrium constant for the intermediate  $\text{HO}\cdot\text{-OH}^{\text{-}}$ .

As for the  $\text{H}_2\text{O}_2$  adsorption, the adsorption of the anion radical on iron oxides/hydroxides is assumed to follow the Langmuir isotherm .

The exact forms of the hydrated intermediates are not known, but since they are negatively charged and in acid-base equilibrium with each other, it is reasonable to assume that the equilibrium concentration of the aqueous species is proportional to  $[\text{OH}^{\text{-}}(\text{aq})]$ . Thus, the phase equilibrium constant can be further simplified to:

$$K_{red}^{ad} = \frac{[\text{OH}^-(\text{aq})]}{[\text{HO}\cdot - \text{OH}^-(\text{ad})]} \quad (15)$$

Finally, to complete the overall reduction process, a fast, irreversible electron transfer process occurs:



For this reaction mechanism, the rate of the reversible first electron transfer step is given by the Butler-Volmer relationship

$$j_c \approx -2 \cdot j_{11}^0 \cdot \left( \exp\left(\frac{-\alpha_{11}F}{RT} \cdot (E - E_{11}^{eq})\right) - \exp\left(\frac{(1-\alpha_{11})F}{RT} \cdot (E - E_{11}^{eq})\right) \right) \quad (17)$$

where  $j_c$  is the net cathodic current density;  $E$  the applied potential;  $E_{11}^{eq}$  the equilibrium potential of reaction (11);  $j_{11}^0$  the exchange current density at  $E_{11}^{eq}$ ;  $\alpha_{11}$  the transfer coefficient for the cathodic reaction (11), typically 0.5; and  $F$  the Faraday constant. When  $E < E_{11}^{eq}$ , the first electron transfer can be considered effectively irreversible and rate-controlling:

$$j_c \approx -2 \cdot j_{11}^0 \cdot \exp\left(\frac{-\alpha_{11}F}{RT} \cdot (E - E_{11}^{eq})\right) \quad (18)$$

The consequence of this combination of a slow and effectively irreversible first electron transfer coupled to a rapid second electron transfer will be to maintain adsorbed surface intermediates at low coverage, justifying the use of a linear isotherm and minimizing the loss of the radical intermediates to solution.

The equilibrium potential for reaction (11) can be expressed as a function of  $[\text{H}_2\text{O}_2(\text{aq})]$  and pH, since

$$E_{11}^{eq} \approx E_{11}^0 + \frac{RT}{F} \ln \frac{[\text{H}_2\text{O}_2(\text{ad})]_{eq}}{[\text{HO}\cdot - \text{OH}^-(\text{ad})]_{eq}} \quad (19)$$

and the adsorbed species are in pH-dependent phase equilibrium with their aqueous equivalents,

$$E_{11}^{eq} \approx E_{11}^{0'} + \frac{RT}{F} \ln \left( \frac{[{}^m\text{H}_2\text{O}_2(\text{aq})]}{[\text{OH}^-(\text{aq})]} \right) \quad (20)$$

where  $E_{11}^{0'} \approx E_{11}^0 + \frac{RT}{F} \ln(K_{red}^{ad} \cdot K_{H_2O_2}^{ad})$ . (21)

Incorporation of equations (20) and (21) into equation (18) yields

$$j_c \approx -2 \cdot j_{11}^0 \cdot \exp \left( \frac{-\alpha_{11} F}{RT} \cdot \left( E - E_{11}^{0'} - \frac{RT}{F} \ln \left( \frac{[{}^m\text{H}_2\text{O}_2(\text{aq})]}{[\text{OH}^-(\text{aq})]} \right) \right) \right), \quad (22)$$

resulting (at 298 K) in

$$\log |j_c| \approx \log j_{11}^{0'} - \frac{1}{118\text{mV}} \cdot (E - 59\text{mV} \times \log [{}^m\text{H}_2\text{O}_2(\text{aq})] + 59\text{mV} \times \text{pH}), \quad (23)$$

where  $\log j_{11}^{0'} \approx \log(2 \cdot j_{11}^0) + \frac{E_{11}^{0'} - 59\text{mV} \times \text{p}K_w^{H_2O}}{118\text{mV}}$  (24)

and  $\text{p}K_w^{H_2O}$  is the acid-base equilibrium constant of water.

By using  $[{}^m\text{H}_2\text{O}_2]$  and the pH-normalized potential,  $E_C^{Norm}$  :

$$E_C^{Norm} = E - 59\text{mV} \times \log [{}^m\text{H}_2\text{O}_2(\text{aq})] + 59\text{mV} \times \text{pH} \quad (25)$$

we can write

$$\log |j_c| \approx \log j_{11}^{0'} - \frac{1}{118\text{mV}} \cdot E_C^{Norm} \quad (26)$$

The proposed mechanism involves a hydroxyl radical as one of the electro-reduction intermediates. However, the proposed mechanism differs from other mechanisms involving Fenton or Fenton-like reactions in that the adsorbed intermediates are in phase equilibrium with  $\text{OH}^-$  in the bulk aqueous phase. The observed pH dependence arises mainly from this pH

dependence of the adsorption-desorption equilibrium for the intermediate products, equation (15). The rate-determining step is the reduction of adsorbed  $\text{H}_2\text{O}_2$  on the  $\alpha\text{-Fe}_2\text{O}_3$  surface, reaction (9), and the 59 mV shift of the plots with pH and  $[\text{H}_2\text{O}_2]$  is attributable to the shift in equilibrium potential for this reaction.

The proposed mechanism is similar, but involves different intermediate steps, to that proposed by Calvo and Schiffrin for the electroreduction of  $\text{H}_2\text{O}_2$  on passive iron (0.4 V vs SCE) at  $\text{pH} > 11$  [15]. They observed similar dependencies on  $[\text{H}_2\text{O}_2]$  and  $[\text{OH}^-]$  but attributed these to a chemical equilibrium process on the passive film prior to electron transfer, and proposed that the reduction occurs on surface  $\text{Fe}^{3+}$  cations, which act as coordinating sites. S. Zečević *et al.* studied hydrogen peroxide reduction on passive iron at  $\text{pH} 8.6 - 13.8$  in borate or unbuffered NaOH solutions, and reported a first order dependence on  $[\text{H}_2\text{O}_2]$ , but no dependence on pH for  $\text{pH} < 11$ , with the reaction becoming pH dependent at  $\text{pH} > 11$  [16]. The authors attributed their pH dependencies partly to the change in molecular  $\text{H}_2\text{O}_2$  concentration, arising from the acid-base equilibrium of  $\text{H}_2\text{O}_2$ , and partly to the pH dependent properties of the passive iron oxide surface. They suggested that, on passive iron, the rate-determining step involves the transfer of the first electron to the molecular  $\text{H}_2\text{O}_2$ , not its base form  $\text{HO}_2^-$ , but did not provide a clear explanation for the pH independence at  $\text{pH} < 11$ . One possibility is that their surface was composed of a mixture of oxides/hydroxides which obscured the clear dependencies observed in this study.

### 3.4 Anodic Oxidation of $\text{H}_2\text{O}_2$ on $\alpha\text{-Fe}_2\text{O}_3$

$\text{Log } |j_a|$  vs  $E$  plots obtained during anodic scans exhibit very different behaviour to those observed on cathodic scans. In Fig. 7, the results for  $\text{pH} 10.6$  (Fig. 7a) and  $[\text{H}_2\text{O}_2] = 1 \times 10^{-3}$  mol-dm $^{-3}$  (Fig. 7c) as typical results are shown. All of other pH and  $[\text{H}_2\text{O}_2]$  exhibits similar

results. The plots were not defined simple Tafel regions like currents were observed during cathodic scans. The plots can be divided into three regions: Region I, from OCP to +150mV, the currents very slowly increase with potential positive scan. Region II, from overpotential +150mV to ~ +300mV, the currents sharply rise with potential positive scan. Region III, from overpotential ~300mV to higher, the currents increases mildly comparing with region II, but still much higher the region I.

For the region I, the current and potential behaviours probably attribute to adsorption or/and desorption steps as reaction determining steps. Adsorption increases the concentrations of active species ( $\text{H}_2\text{O}_2$ ) and with surface catalysis effects, decreasing the activation energy of  $\text{H}_2\text{O}_2$  oxidizing, making the  $\text{H}_2\text{O}_2$  oxidation at lower potentials. The reactions are reaction 4.

Equilibrium potential of molecular  $\text{H}_2\text{O}_2$  is  $-0.14\text{V}$  (pH 10.6,  $[\text{H}_2\text{O}_2] = 10^{-3}\text{ M}$ ). Since point of zero charge for  $\alpha\text{-Fe}_2\text{O}_3$  is 6.5 [32], at pH range of our study, 9.2 – 12.6, the surface of  $\alpha\text{-Fe}_2\text{O}_3$  is negative charge. Neutral  $\text{H}_2\text{O}_2$  moleculars probably are easier adsorption on the  $\alpha\text{-Fe}_2\text{O}_3$  surface than its conjugate base  $\text{HO}_2^-$ . Since adsorption increasing  $[\text{H}_2\text{O}_2]$  on the surface, when the potential scan from OCP to positive, adsorptional molecular  $\text{H}_2\text{O}_2$  is oxidized at lower potential than equilibrium potentials calculated from buck solution  $[\text{H}_2\text{O}_2]$ . Due to reaction is controlled by adsorption, the  $\text{H}_2\text{O}_2$  surface concentration dependent on the available sites on the surface, the current is near constant and higher,  $\sim 10^{-7}\text{ A}\cdot\text{cm}^{-2}$  since higher surface concentrations and coverage close to 1. Along with potential rising, the electrode surface potential higher enough for  $\text{H}_2\text{O}_2$  oxidation from buck solution. The current increases sharply with potential scan since all of surface (such as non-adsorption sites) is available for oxidation and reaction turn to electron transfer control. This gives an explanation of current and potential behaviours in region I and II. For region III, the current behaviour at  $E > E_{\text{OC}} + 0.3\text{ V}$  is likely significantly influenced

by water oxidation and active species diffusion, and not used in the following analysis. From our explanation, we can predict the plots will be overlap each other if the plots were shift  $0.059 \text{ pH}^{-1}$  as we did at  $\text{H}_2\text{O}_2$  reduction section because the reaction is are pH dependent. And we can predict in region II, the Tafel slopes should be close to  $118 \text{ mV}\cdot\text{dec}^{-1}$ , agree with the Tafel slopes observed to be  $126 \pm 10 \text{ mV}\cdot\text{dec}^{-1}$  at higher  $[\text{H}_2\text{O}_2]$   $5 \times 10^{-3} - 10^{-2} \text{ M}$ . At lower  $[\text{H}_2\text{O}_2]$ , the Tafel slopes were observed to be  $169 \pm 10 \text{ mV}\cdot\text{dec}^{-1}$ , probably due to at lower  $[\text{H}_2\text{O}_2]$ ,  $\text{H}_2\text{O}_2$  oxidizing currents in region I making large influence for region II, resulting currents to deviate one electron transfer Tafel behaviours.

As for the cathodic reaction, the plots can be made to overlap by shifting along the potential axis by  $-59 \text{ mV}$  per  $\log [\text{H}_2\text{O}_2]$  and  $+59 \text{ mV}$  per pH unit. Again, the data for pH 10.6 and  $1 \times 10^{-3} \text{ mol}\cdot\text{dm}^{-3} [\text{H}_2\text{O}_2]$  are used as the reference set for this adjustment. Of note is the direction of potential shift required with respect to  $[\text{H}_2\text{O}_2]$  which is opposite to that of the cathodic scan, although the pH dependence shifts in the same direction. Also, as before, the data for pH 11.5 and 12.6 require additional shifts of  $11 \text{ mV}$  and  $54 \text{ mV}$ , respectively, to obtain the overlapping plots shown in Fig. 7b and 7d. These observations indicate that, as for the cathodic reaction, only the molecular form of  $\text{H}_2\text{O}_2$  is electroactive, that similar adsorption-desorption equilibria of intermediates are involved, and that the influence of  $[\text{H}_2\text{O}_2]$  and pH on the equilibrium potential determines the locations of the profiles on the potential axis.

For all  $[\text{H}_2\text{O}_2]$  at region II, the Tafel slope of  $116 \sim 180 \text{ mV}\cdot\text{dec}^{-1}$  is significantly wide and deviated the  $118 \text{ mV}\cdot\text{dec}^{-1}$  expected for rate control by a one-electron transfer. However, as discussion above, at higher  $[\text{H}_2\text{O}_2]$ , the Tafel slopes are close to  $118 \text{ mV}\cdot\text{dec}^{-1}$  suggesting the first electron transfer is totally rate-controlling. Since this first electron transfer will involve a temporary reduction of  $\text{Fe}^{\text{III}}$  to  $\text{Fe}^{\text{II}}$  in the electrode surface this would indicate that the

electrochemical regeneration of  $\text{Fe}^{\text{III}}$  is more rapid than the electrochemical regeneration of  $\text{Fe}^{\text{II}}$  in the cathodic reaction case. This is consistent with the observation (Figure 2) that  $E_{\text{OC}}$  is closer to  $E_{\text{O}_2/\text{H}_2\text{O}_2}^{\text{eq}}$  than  $E_{\text{H}_2\text{O}_2/\text{OH}^-}^{\text{eq}}$ , indicating that the open-circuit decomposition reaction involving the coupling of the anodic and cathodic half reactions is controlled by the anodic reaction. Due to adsorption keeps the  $[\text{H}_2\text{O}_2]$  nearly constants, increasing the  $[\text{H}_2\text{O}_2]$  will insignificant influence the reaction rate of  $\text{H}_2\text{O}_2$ , but will accelerate  $\text{H}_2\text{O}_2$  reduction rates. OCPs will slightly raised to more positive potentials with  $[\text{H}_2\text{O}_2]$ , consistence of experimental observation from Fig. 2.

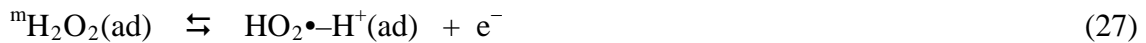
$\text{H}_2\text{O}_2$  adsorption on surface makes the reaction mechanism complicated, however, one electron transfer control Tafel relationship of current and potential profiles are obvious in region II, particular in higher  $[\text{H}_2\text{O}_2]$ . An analysis of reaction mechanism should be reasonable, similar to that proposed for the reduction of  $\text{H}_2\text{O}_2$ . The analysis of mechanism in region II can give suggestions for reaction mechanism in region I, although it is very complex and can not be analyzed now.

The mechanism in region II can be constructed for the oxidation of  $\text{H}_2\text{O}_2$ , Figure 8:



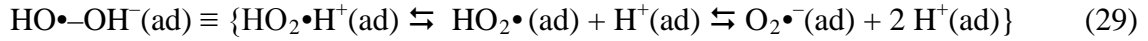
(9)

$$K_{\text{H}_2\text{O}_2}^{\text{ad}} = \frac{[{}^m\text{H}_2\text{O}_2(\text{ad})]}{[{}^m\text{H}_2\text{O}_2(\text{aq})]} \quad (10)$$



Although the formation of the superoxide radical,  $\text{O}_2\bullet^-$ , on the hydroxide surface cannot be confirmed, its formation by the reaction of  $\text{H}_2\text{O}_2$  with  $\text{Fe}^{3+}$  is well established .

As for the cathodic case, the adsorbed intermediate products,  $\text{HO}_2\cdot\text{-H}^+(\text{ad})$ , represent a range of oxidized  $\text{H}_2\text{O}_2$  species from a hydrogen peroxide cation radical,  $\text{HO}_2\cdot\text{H}^+$ , to the dissociated pairs,  $\text{HO}_2\cdot/\text{H}^+$  or  $\cdot\text{O}_2^-/2 \text{H}^+$ :



As for the reduction case, these intermediate surface species are assumed to be in adsorption-desorption equilibrium with their aqueous equivalents:



and, although the exact forms of the hydrated intermediates are not known, their concentration is assumed to be proportional to  $[\text{H}^+(\text{aq})]$  (not  $[\text{OH}^-(\text{aq})]$  as in the cathodic case) so that:

$$K_{ox}^{ad} = \frac{[\text{H}^+(\text{aq})]}{[\text{HO}_2\cdot\text{-H}^+(\text{ad})]} \quad (31)$$

Again, the adsorption of the intermediate superoxide and its acid form is assumed to follow the linear adsorption isotherm. Previous studies on the adsorption of various species on iron oxides have shown that while anion adsorption follows the Langmuir isotherm, cation adsorption more closely follows the Freundlich isotherm. The consequence of assuming a simple Langmuir adsorption isotherm is discussed in detail later.

Assuming the first electron transfer, reaction (27), is rate determining, the current-potential profile can be obtained by a similar analysis to that used for  $\text{H}_2\text{O}_2$  reduction. The main difference comes from the equilibrium potential of the rate determining step, in this case, reaction (27):

$$E_{27}^{eq} \approx E_{27}^0 + \frac{RT}{F} \ln \frac{[\text{HO}_2\cdot\text{-H}^+(\text{ad})]}{[{}^m\text{H}_2\text{O}_2(\text{ad})]} \quad (32)$$

and the equilibrium of the adsorbed species with aqueous species,

$$E_{27}^{eq} \approx E_{27}^{0'} + \frac{RT}{F} \ln \left( \frac{[\text{H}^+(\text{aq})]}{[\text{mH}_2\text{O}_2(\text{aq})]} \right), \quad (33)$$

where  $E_{27}^{0'} \approx E_{27}^0 - \frac{RT}{F} \ln(K_{ox}^{ad} \cdot K_{\text{H}_2\text{O}_2}^{ad})$  (34)

This results in (at 298 k)

$$\log |j_a| \approx \log j_{27}^{0'} - \frac{1}{118 \text{ mV}} \cdot (E + 59 \text{ mV} \times \log [\text{mH}_2\text{O}_2(\text{aq})] + 59 \text{ mV} \times \text{pH}) \quad (35)$$

where  $\log j_{27}^{0'} \approx \log(2 \cdot j_{27}^0) + \frac{E_{25}^{0'}}{118 \text{ mV}}$  (36)

By using  $[\text{mH}_2\text{O}_2]$  and a pH normalized potential,  $E_A^{Norm}$  :

$$E_A^{Norm} = E + 59 \text{ mV} \times \log [\text{mH}_2\text{O}_2(\text{aq})] + 59 \text{ mV} \times \text{pH} \quad (37)$$

and  $\log |j_a| \approx \log j_{27}^{0'} - \frac{1}{118 \text{ mV}} \cdot E_A^{Norm}$  (38)

This analysis predicts a Tafel slope of 118 mV·dec<sup>-1</sup> (compared to the observed value of 116 ± 10 mV·dec<sup>-1</sup> at higher [H<sub>2</sub>O<sub>2</sub>]) independent of pH and [mH<sub>2</sub>O<sub>2</sub>(aq)]. The proposed mechanism predicts a – 59 mV dependence of the log current-potential profile on [mH<sub>2</sub>O<sub>2</sub>(aq)] at a given pH and +59 mV dependence on pH. The observed dependence on pH follows the prediction very well (Fig. 7d), but the observed dependence on [mH<sub>2</sub>O<sub>2</sub>(aq)] deviates somewhat from the prediction (Fig. 7b) (see further discussion below). Nevertheless, the proposed mechanism accounts for the first order dependencies on [OH<sup>-</sup>] and near first order dependence on [mH<sub>2</sub>O<sub>2</sub>]. Note that the H<sub>2</sub>O<sub>2</sub> reduction has an *inverse* first-order dependence on [OH<sup>-</sup>].

That the observed Tafel slopes are higher than predicted for the proposed mechanism at lower [H<sub>2</sub>O<sub>2</sub>] in region II, may be attributed to the fact that the first electron transfer is not totally rate-controlling as assumed at lower [H<sub>2</sub>O<sub>2</sub>] as discussion above. However, it could be

partially due to the simplistic assumption of a linear dependence of the adsorption isotherm for the intermediates,  $\text{HO}_2\bullet\text{-H}^+(\text{ad})$ , on  $[\text{H}^+(\text{aq})]$ , equation (28), as can be judged from the less perfect overlap of  $\log |j_a|$  vs  $E$  plots at lower  $[\text{H}_2\text{O}_2]$ , Figure 7b.

Studies on  $\text{H}_2\text{O}_2$  oxidation on iron oxides are rare. Gojivic *et al* studied hydrogen peroxide oxidation on passive iron (0.5 V vs SCE) at pHs between 9.8 and 13.8 in borate and unbuffered NaOH solutions [30] and reported a Tafel slope of  $\sim 110 \text{ mV}\cdot\text{dec}^{-1}$  and reaction orders of 0.5 with respect to  $\text{H}_2\text{O}_2$  and 0.7 with respect to  $\text{OH}^-$ . The difference between the work by S. Zečević *et al* and ours is likely due to different oxide surface compositions. The passive iron surface formed at 0.5 V vs SCE between pH 9.8 and 13.8 is expected to be a mixture of several iron oxides and/or oxyhydroxides [16], each of which could have different catalytic reactivities for  $\text{H}_2\text{O}_2$  oxidation, resulting in fractional reaction orders with respect to  $\text{H}_2\text{O}_2$  and  $\text{OH}^-$ .

### 3.5 *$\text{H}_2\text{O}_2$ Decomposition Current on $\alpha\text{-Fe}_2\text{O}_3$ Surface*

Regardless of individual mechanisms for the electrochemical oxidation and reduction of  $\text{H}_2\text{O}_2$ , the intersection of extrapolated Tafel relationships yields the  $\text{H}_2\text{O}_2$  decomposition current density,  $|j_d|$ . Figure 9 shows such two extrapolations of the data obtained at pH 10.6 for  $[\text{H}_2\text{O}_2]$  ranging from  $5 \times 10^{-4}$  to  $10^{-2} \text{ mol}\cdot\text{dm}^{-3}$  from electrochemical reduction and oxidation (region I and II). Due to surface adsorption and catalysis effects, Tafel slopes are different in region I and II.  $\text{H}_2\text{O}_2$  decomposition currents ( $|j_d(\text{I})|$  and  $|j_d(\text{II})|$ ) from two intersections were obtained from extrapolation in region I and II. The  $\text{H}_2\text{O}_2$  decomposition currents obtained from these intersections are presented as a function of pH and  $[\text{H}_2\text{O}_2]$  in Figure 10a and 10b, respectively. The slopes of the log-log plots provide the reaction orders with respect to  $[\text{OH}^-]$  and  $[\text{H}_2\text{O}_2]$ ,

respectively. The results show that both of the  $\text{H}_2\text{O}_2$  decomposition rates are nearly independent of pH and  $[\text{H}_2\text{O}_2]$ .

Decomposition currents from extrapolation of region II and reduction are smaller than from region I as expected since adsorption maybe increase  $[\text{H}_2\text{O}_2]$  on the surface making the oxidation reaction faster.

Since  $\text{H}_2\text{O}_2$  decomposition on  $\alpha\text{-Fe}_2\text{O}_3$  shows a zero-order dependence on  $[\text{H}_2\text{O}_2(\text{aq})]$ , the surface reaction kinetic equation can be expressed as:

$$-\left. \frac{d[\text{H}_2\text{O}_2]}{dt} \right|_{\text{Surface}} = \frac{|j_d|}{nF} = k_{\text{obs}} \quad (36)$$

where  $n$  is the total number of electrons involved in the electrochemical decomposition, equal to 2 in this case, and  $k_{\text{obs}}$  is a rate coefficient for the surface decomposition of  $\text{H}_2\text{O}_2$  (denote  $k_{\text{obs}}(\text{I})$  and  $k_{\text{obs}}(\text{II})$  from decomposition currents ( $|j_d|(\text{I})$  and  $|j_d|(\text{II})$ ). The bulk aqueous phase concentration of  $\text{H}_2\text{O}_2$  does not change over the duration of these experiments allowing the decomposition rate constant to be determined from the decomposition current,  $j_d$ .

The  $k_{\text{obs}}$  determined from  $j_d$  is very low ( $8 \pm 2 \times 10^{-13}$  and  $2 \pm 2 \times 10^{-13} \text{ mol}\cdot\text{cm}^{-2}\cdot\text{s}^{-1}$  for  $k_{\text{obs}}(\text{I})$  and  $k_{\text{obs}}(\text{II})$ , respectively), indicating that the  $\alpha\text{-Fe}_2\text{O}_3$  surface is a poor catalyst for  $\text{H}_2\text{O}_2$  decomposition. No  $\text{H}_2\text{O}_2$  decomposition rates on  $\alpha\text{-Fe}_2\text{O}_3$  were reported in the pH range we did in literatures. Some researcher reported decompositiopn reaction is first order for  $\text{H}_2\text{O}_2$  in acidic and neutral environments. The reaction rates are  $0.2 - 1 \times 10^{-13} \text{ mol}\cdot\text{cm}^{-2}\cdot\text{s}^{-1}$  for  $10^{-3} \text{ mol}\cdot\text{dm}^{-3}$   $[\text{H}_2\text{O}_2]$  [34-35]. These results are close the rates measured in our study for region II decomposition rates although the reactions are in different reaction orders due to various reaction mechanisms. Decomposition rate in region I is an order of magnitude higher than those reported

probably due to different reaction mechanism in acidic and base solutions and adsorption increasing the  $[H_2O_2]$ .

### **Conclusion:**

The electrochemical reduction and oxidation kinetics of hydrogen peroxide on  $\alpha\text{-Fe}_2\text{O}_3$  films chemically deposited on indium tin oxide substrates were studied over the pH range of 9.2 to 12.6 and the  $[H_2O_2]$  range of  $10^{-4}$  to  $10^{-2}$  mol·dm<sup>-3</sup>. The Tafel slopes for  $H_2O_2$  reduction and oxidation obtained from polarization measurements are  $124 \pm 6$  and are independent of pH and the concentration of  $H_2O_2$ .  $H_2O_2$  oxidation reactions are adsorption behaviours, currents slightly increasing with potentials at lower overpotentials, and rapidly increasing with Tafel behaviours at higher overpotentials.

The reduction of  $H_2O_2$  has a first order dependence on the concentration of the molecular  $H_2O_2$  and an inverse first order dependence on the concentration of  $OH^-$ . A mechanism consistent with these observations, is proposed, and involves adsorbed  $HO\bullet$  and its base,  $HO\bullet OH^-$ , as intermediates. These intermediates are in adsorption-desorption equilibrium with  $OH^-$  in the bulk aqueous phase, thus contributing to the observed dependence of the rate on pH. The electroactive species is the molecular  $H_2O_2$ , not its base form,  $HO_2^-$  and the charge transfer rate-determining step is the reduction of adsorbed  $H_2O_2$ , a reaction which utilizes  $Fe^{III}/Fe^{II}$  sites in the  $\alpha\text{-Fe}_2\text{O}_3$  surface as an electron donor-acceptor relay.

The electrochemical oxidation  $H_2O_2$  has first order dependencies on  $[^mH_2O_2]$  and  $[OH^-]$ . A similar mechanism to that proposed for  $H_2O_2$  reduction is proposed; this involves radical intermediates, but for the oxidation, these intermediates consist of  $HO_2\bullet H^+$ ,  $HO_2\bullet$ , and  $\bullet O_2^-$ . These intermediates are in adsorption-desorption equilibrium with  $H^+$  in the bulk aqueous phase,

giving the observed pH dependence. The rate-determining step is the  $\text{Fe}^{\text{III}}/\text{Fe}^{\text{II}}$  site-assisted oxidation of adsorbed  $\text{H}_2\text{O}_2$  to the intermediates, and the electroactive species is the molecular  $\text{H}_2\text{O}_2$ , not its base form,  $\text{HO}_2^-$ .

The decomposition rate of  $\text{H}_2\text{O}_2$  on  $\alpha\text{-Fe}_2\text{O}_3$  was determined by extrapolation of Tafel relationships to  $E_{\text{OC}}$ , and is zero order with respect to  $[\text{H}_2\text{O}_2(\text{aq})]$ , but pH independent. The decomposition rate constant was determined to be  $8 \pm 2 \times 10^{-13} \text{ mol}\cdot\text{cm}^{-2}\cdot\text{s}^{-1}$ , indicating that the  $\alpha\text{-Fe}_2\text{O}_3$  surface is a poor catalyst for  $\text{H}_2\text{O}_2$  decomposition.

### ***Acknowledgements:***

This research was funded under the Natural Science and Engineering Council of Canada (NSERC) and Atomic Energy of Canada Limited (AECL) Industrial Research Chair Agreement. The electrochemical analysis equipment was purchased by a grant from the Canada Foundation for Innovation.

### **REFERENCES**

- [1] J.W.T. Spinks, R.J. Woods, An introduction to radiation chemistry 3rd ed., Wiley, New York, 1990.
- [2] I.G. Draganić, Z.D. Draganić, The radiation chemistry of water Academic Press, New York, 1971.
- [3] J.M. Joseph, B.S. Choi, P. Yakabuskie, J.C. Wren, Radiation Physics and Chemistry 77 (2008) 1009.
- [4] K. Daub, X. Zhang, J.J. Noel, J.C. Wren, Electrochimica Acta 55 (2009) 2767.
- [5] S. Uchida, T. Satoh, J. Sugama, N. Yamashiro, Y. Morishima, T. Hirose, T. Miyazawa, Y. Satoh, K. Iinuma, Y. Wada, M. Tachibana, Journal of Nuclear Science and Technology 42 (2005) 66.
- [6] B.P.J. Isabey, B. Hickel, Journal of Nuclear Materials 264 (1999) 309.
- [7] W. Xu, K. Daub, X. Zhang, J.J. Noel, D.W. Shoesmith, J.C. Wren, Electrochim. Acta 54 (2009) 5727.
- [8] D.W. Shoesmith (Ed.), ASM Handbook Vol. 13A(Corrosion), ASM International., 2003.
- [9] T. Jonsson, B. Pujilaksono, S. Hallström, J. Ågren, J.-E. Svensson, L.-G. Johansson, M. Halvarsson, Electrochimica Acta 51 (2009) 1914.

- [10] H.P. Hermansson, G. Persson, A. Reinvall, *Nuclear Technology* 103 (1999) 101.
- [11] I.A. Salem, M. El-Maazawi, A.B. Zaki, *International Journal of Chemical Kinetics* 32 (2000) 643.
- [12] E. Yeager, P. Krouse, K.V. Rao, *Electrochimica Acta* 18 (1964) 1057.
- [13] C.-C. Chang, T.-C. Wen, H.-J. Tien, *Electrochimica Acta*, 42 (1997) 557.
- [14] V.G. Prabhuu, L.R. Zarakara, R.G. Dhaneshwara, *Electrochimica Acta* 26 (1981) 725.
- [15] E.J. Calvo, D.J. Schiffrina, *Journal of Electroanalytical Chemistry* 163 (1984) 257.
- [16] S. Zečević, D.M. Dražić, S. Gojković, *Electrochimica Acta* 36 (1991) 5.
- [17] N.D. Merkulova, G.V. Zhutaeva, N.A. Shumilova, V.S. Bagotzky, *Electrochimica Acta* 18 (1973) 169.
- [18] E.R. Vago, E.J. Calvo, *Journal of Electroanalytical Chemistry* 339 (1992) 41.
- [19] B. Wu, H. Lei, C. Cha, Y. Chen, *Journal of Electroanalytical Chemistry* 377 (1994) 227.
- [20] A.L.-T. Pham, C. Lee, F.M. Doyle, D.L. Sedlak, *Environ Sci Technol* 43 (2009) 8930.
- [21] E. Brillas, I. Sire's, M.A. Oturan, *Chem Rev* 109 (2009) 6570.
- [22] S.S. Lin, M.D. Gurol, *Environ Sci Technol* 32 (1998) 1417.
- [23] G.R. Peyton, O.J. Bell, E. Girin, M.H. LeFavre, *Environ Sci Technol* 29 (1995) 1710.
- [24] J.D. Laat, H. Gallard, *Environ Sci Technol* 33 (1999) 2726.
- [25] J.J. Pignatello, *Environ Sci Technol* 26 (1992) 944.
- [26] E. Lipczynska-Kochany, J. Kochany, *Chemosphere* 73 (2008) 745.
- [27] G.V. Buxton, C.L. Greenstock, W.P. Helman, A.B. Ross, *Journal of physical and chemical reference data* 17 (1988) 513.
- [28] M.C. Gonzalez, D.O. Martire, *International Journal of Chemical Kinetics* 29 (1997) 589.
- [29] B.A. Smith, A.L. Teel, R.J. Watts, *Environ Sci Technol* 38 (2004) 5465.
- [30] S.L. Gojković, S.K. Zečević, D.M. Dražić, *Electrochimica Acta* 37 (1992) 1845.
- [31] D. Fu, J.C. Wren, *Journal of Nuclear Materials* 374 (2008) 116.
- [32] R.M. Cornell, U. Schwertmann (Eds.), *The Iron Oxides, Structure, Properties, Reactions, Occurrences and Uses*, Chapter 11, 2nd Ed ed., Wiley-VCH, 2003.
- [33] C.W. Jones (Ed.), *Applications of hydrogen peroxide and derivatives*, Royal Society of Chemistry, Cambridge, UK, 1999.
- [34] M. Hermanek, R. Zboril, I. Medrik, J. Pechousek, C. Gregor, *Journal of American Chemical Society* 129 (2007) 10929.
- [35] A.L. Teel, D.D. Finn, J.T. Schmidt, L.M. Cutler, R.J. Watts, *Journal of Environmental Engineering* 133 (2007) 853.

## FIGURE CAPTIONS

- Figure 1:** Scanning Electron Micrograph images of (a) the surface and (b) the cross section, and (c) the Raman and (d) XRD spectra of the  $\alpha$ -Fe<sub>2</sub>O<sub>3</sub> film deposited on the ITO glass. Also shown in (c) and (d) are the spectra of the standard samples of iron oxides/hydroxides: 1, the  $\alpha$ -Fe<sub>2</sub>O<sub>3</sub> film used in this study; 2, lepidocrocite ( $\gamma$ -FeOOH); 3, magnetite (Fe<sub>3</sub>O<sub>4</sub>); 4, goethite ( $\alpha$ -FeOOH); and 5, hematite ( $\alpha$ -Fe<sub>2</sub>O<sub>3</sub>).
- Figure 2:** Open circuit potential as a function of pH recorded on the  $\alpha$ -Fe<sub>2</sub>O<sub>3</sub> film on the ITO electrode at various concentrations of H<sub>2</sub>O<sub>2</sub>; 0 mol·dm<sup>-3</sup> (□), 5 × 10<sup>-4</sup> mol·dm<sup>-3</sup> (■), 1 × 10<sup>-3</sup> mol·dm<sup>-3</sup> (●), 5 × 10<sup>-3</sup> mol·dm<sup>-3</sup> (▲) and 1 × 10<sup>-2</sup> mol·dm<sup>-3</sup> (▼). The other lines are the calculated equilibrium potentials for various redox pairs.
- Figure 3:** Linear polarization curves recorded on  $\alpha$ -Fe<sub>2</sub>O<sub>3</sub> in H<sub>2</sub>O<sub>2</sub>-free solutions at various pH values at potential scan rate 0.17 mV·s<sup>-1</sup>.
- Figure 4:** The log current-potential profiles observed during cathodic and anodic scans on  $\alpha$ -Fe<sub>2</sub>O<sub>3</sub> at pH 10.6 solution; the upper panel, a) and b), shows the current without baseline-current correction, and the lower panel, c) and d), with baseline-current correction. [H<sub>2</sub>O<sub>2</sub>] are 5 × 10<sup>-4</sup> mol·dm<sup>-3</sup> (■), 1 × 10<sup>-3</sup> mol·dm<sup>-3</sup> (●), 5 × 10<sup>-3</sup> mol·dm<sup>-3</sup> (▲) and 1 × 10<sup>-2</sup> mol·dm<sup>-3</sup> (▼).
- Figure 5:** Polarization curves observed for H<sub>2</sub>O<sub>2</sub> reduction on a  $\alpha$ -Fe<sub>2</sub>O<sub>3</sub> film; (a) and (b) as a function of [H<sub>2</sub>O<sub>2</sub>] at pH 10.6, and (c) and (d) as a function of pH at 1 × 10<sup>-3</sup> mol·dm<sup>-3</sup> H<sub>2</sub>O<sub>2</sub>. For the lower panel, (b) and (d), the log |j<sub>c</sub>| vs E plots are shifted by -59 mV per log [H<sub>2</sub>O<sub>2</sub>], and 59 mV per pH, with respect to the reference case,

pH 10.6 and  $1 \times 10^{-3} \text{ mol}\cdot\text{dm}^{-3} \text{ H}_2\text{O}_2$ . For pH 11.5 and 12.6 the curves are further corrected for molecular  $\text{H}_2\text{O}_2$  concentration (see the text for details).

**Figure 6:** Schematics of the mechanism proposed for  $\text{H}_2\text{O}_2$  reduction on a  $\alpha\text{-Fe}_2\text{O}_3$  film.

**Figure 7:** Polarization curve observed for  $\text{H}_2\text{O}_2$  oxidation on a  $\alpha\text{-Fe}_2\text{O}_3$  film; (a) and (b) as a function of  $[\text{H}_2\text{O}_2]$  at pH 10.6, and (c) and (d) as a function of pH at  $1 \times 10^{-3} \text{ mol}\cdot\text{dm}^{-3} \text{ H}_2\text{O}_2$ . For the lower panel, (b) and (d), the  $\log |j_c|$  vs E plots are shifted by  $-59 \text{ mV}$  per  $\log [\text{H}_2\text{O}_2]$ , and  $-59 \text{ mV}$  per pH, with respect to the reference case, pH 10.6 and  $1 \times 10^{-3} \text{ mol}\cdot\text{dm}^{-3} \text{ H}_2\text{O}_2$ . For pH 11.5 and 12.6 the curves are further corrected for molecular  $\text{H}_2\text{O}_2$  concentration (see the text for details).

**Figure 8:** Schematics of the mechanism proposed for  $\text{H}_2\text{O}_2$  oxidation on a  $\alpha\text{-Fe}_2\text{O}_3$  film.

**Figure 9:** Determination of the  $\text{H}_2\text{O}_2$  decomposition rate on  $\alpha\text{-Fe}_2\text{O}_3$  from the intersection of Tafel lines obtained for  $\text{H}_2\text{O}_2$  reduction and oxidation.

**Figure 10:**  $\text{H}_2\text{O}_2$  decomposition current; (a) as a function of pH at  $[\text{H}_2\text{O}_2] = 5 \times 10^{-4} \text{ mol}\cdot\text{dm}^{-3}$  (■),  $1 \times 10^{-3} \text{ mol}\cdot\text{dm}^{-3}$  (●),  $5 \times 10^{-3} \text{ mol}\cdot\text{dm}^{-3}$  (▲) and  $1 \times 10^{-2} \text{ mol}\cdot\text{dm}^{-3}$  (▼) for non adsorption and (b) as a function of  $[\text{H}_2\text{O}_2]$  at pH = 9.2 (■), 10.6 (●), 11.5 (▲) and 12.6 (▼). Solid lines for non adsorption; dash line for adsorption

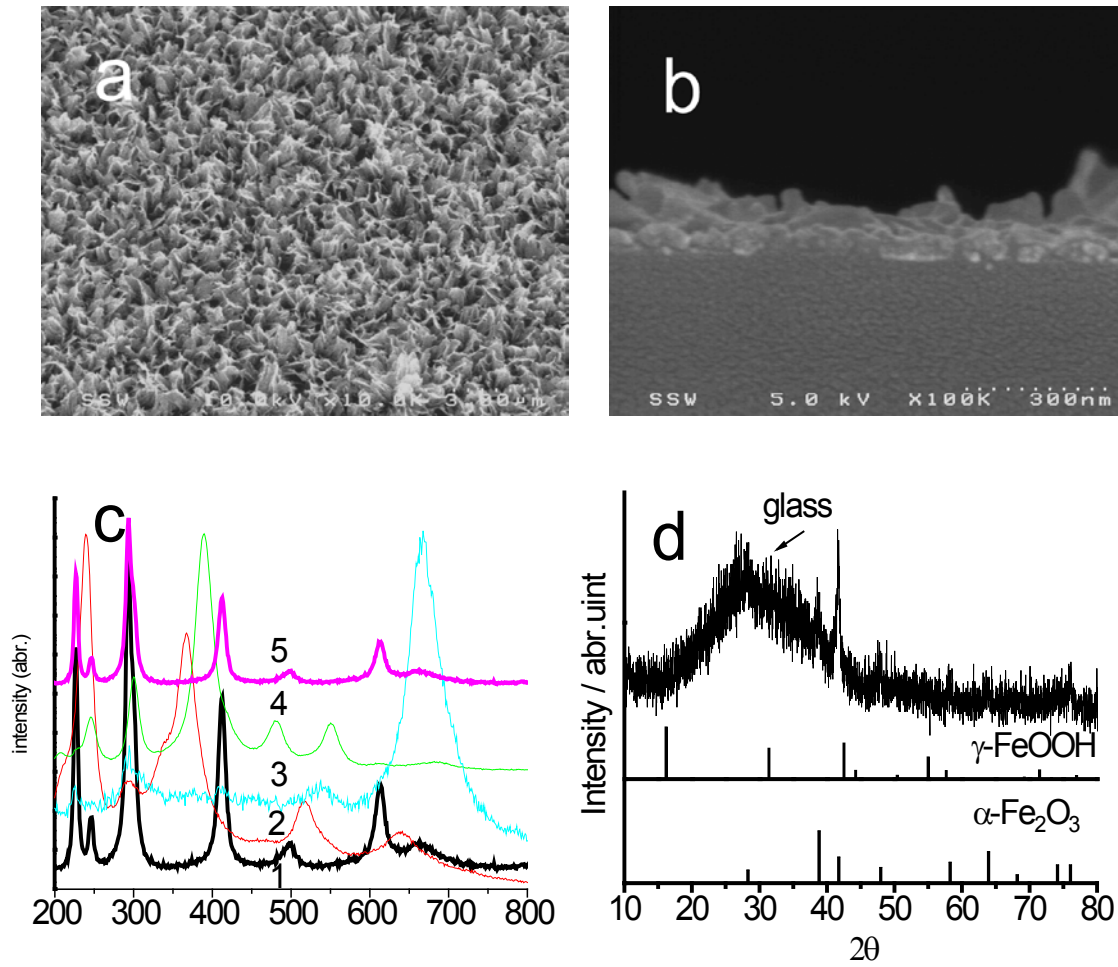


**Figure 1:**

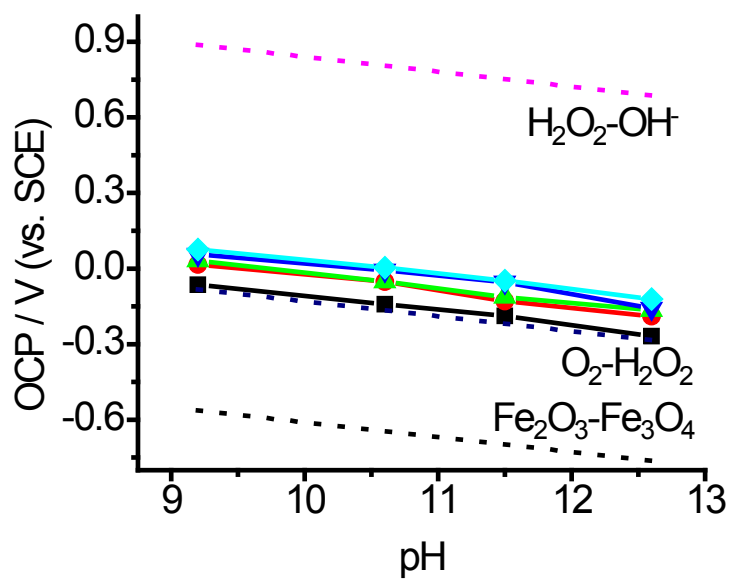
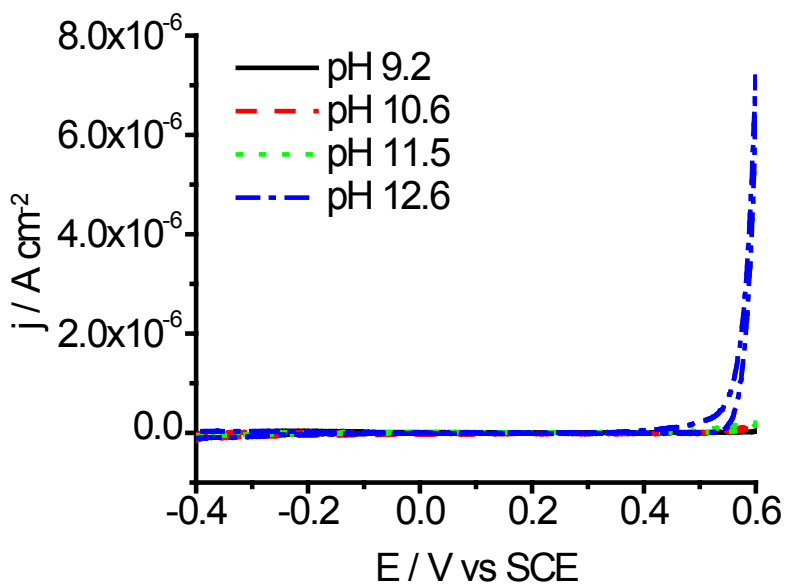
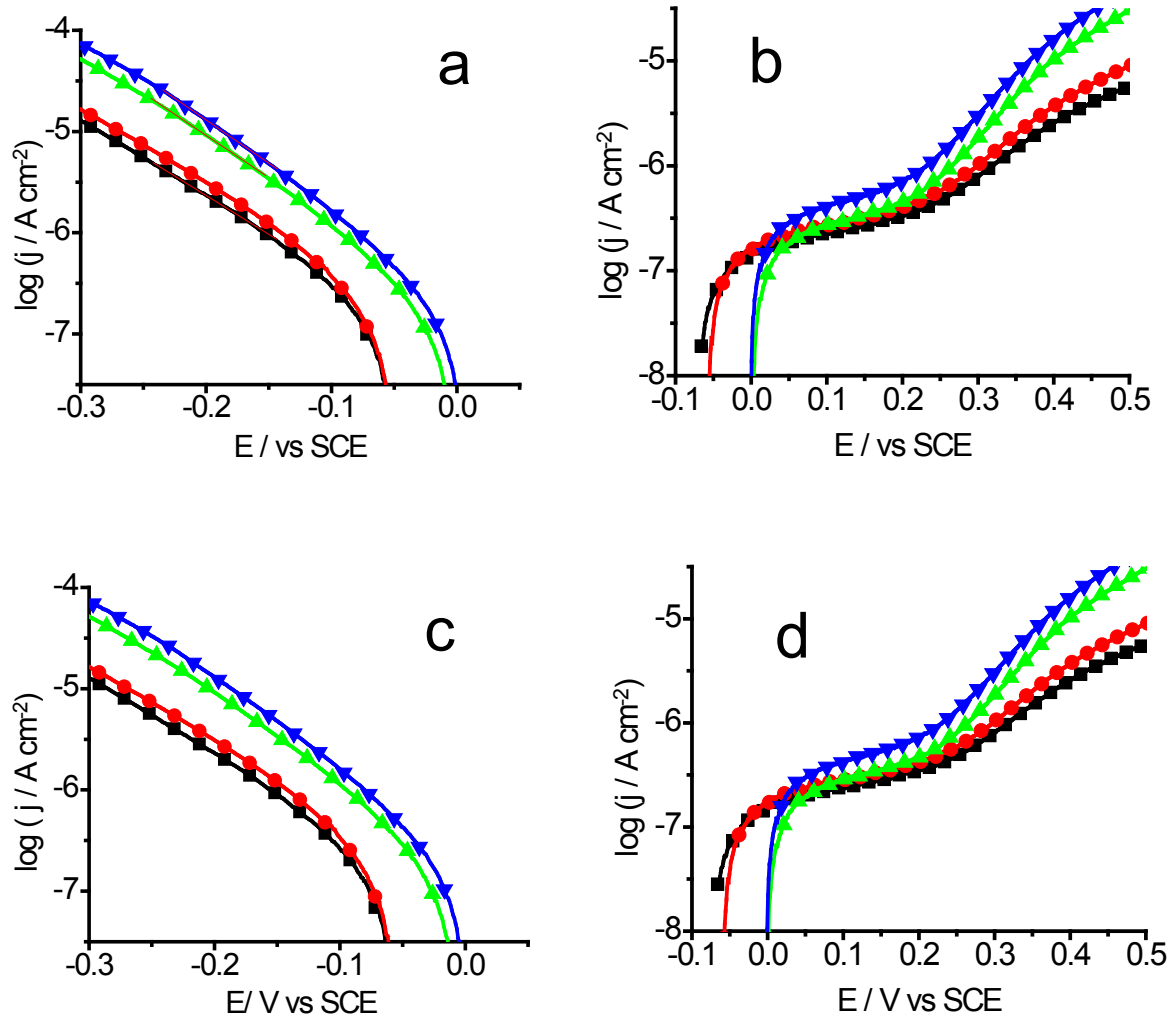


Figure 2:



**Figure 3:**



**Figure 4:**

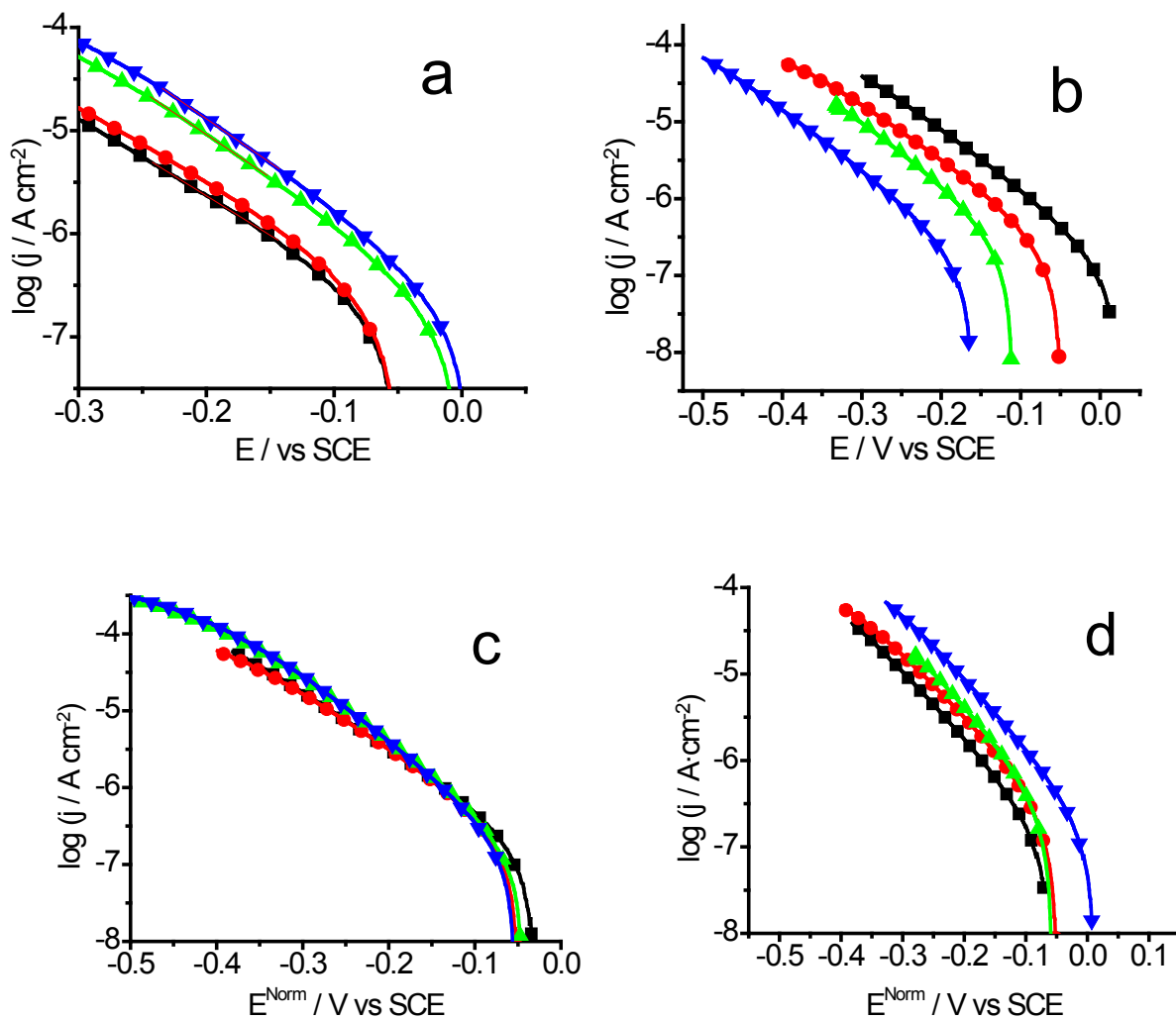


Figure 5:

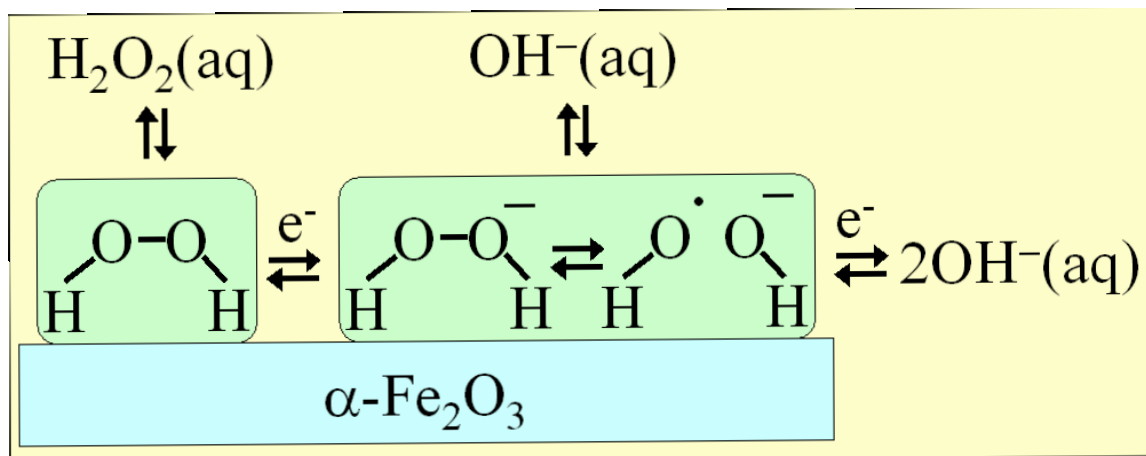


Figure 6:

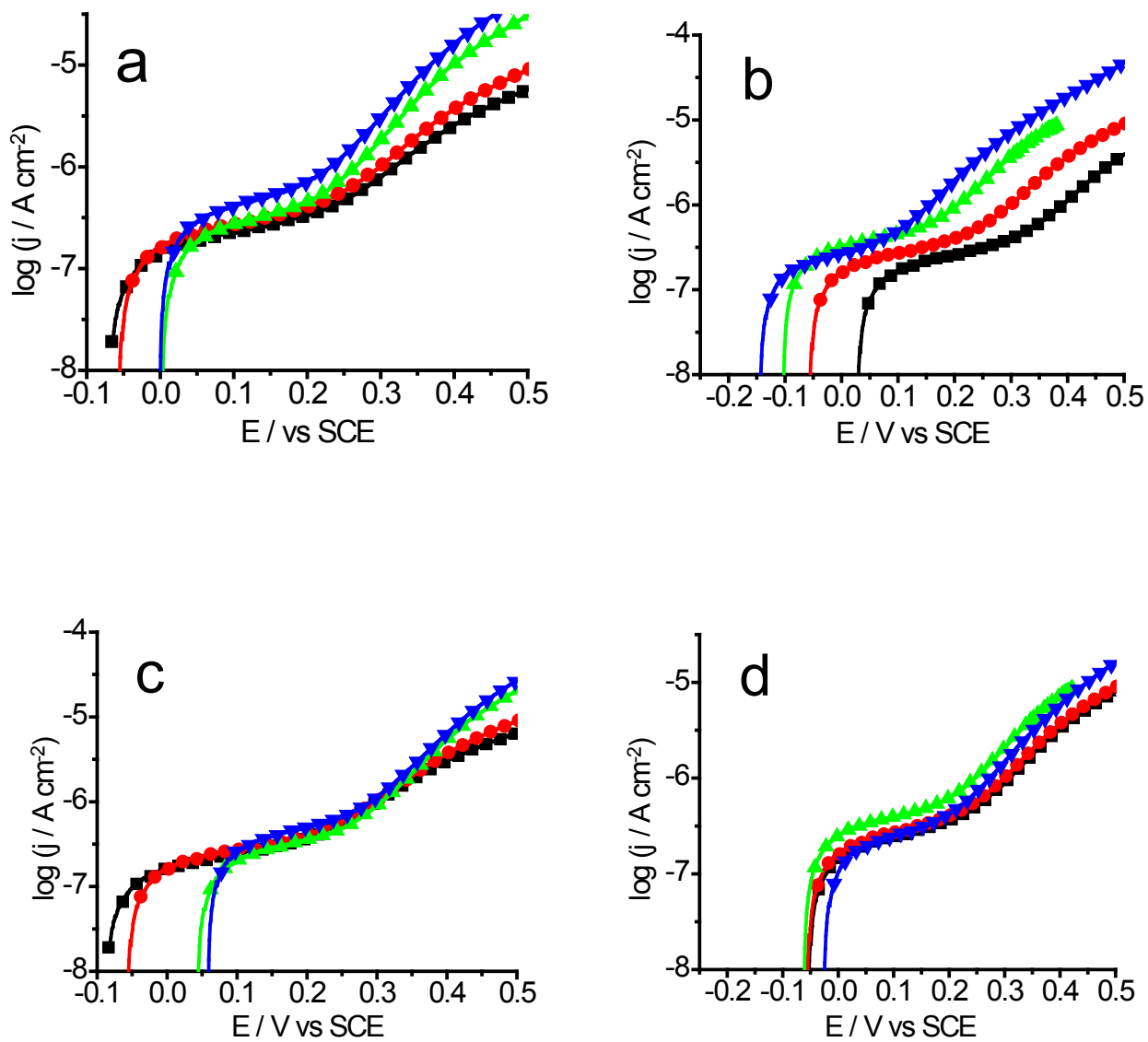


Figure 7:



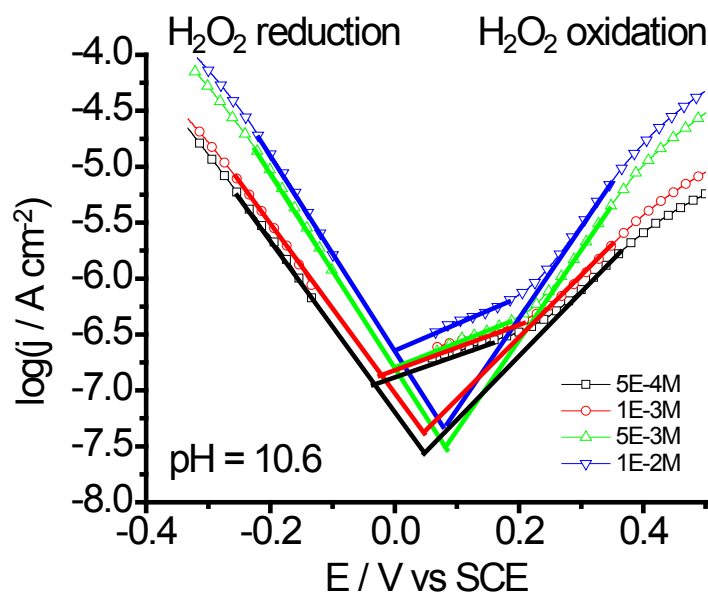


Figure 9:

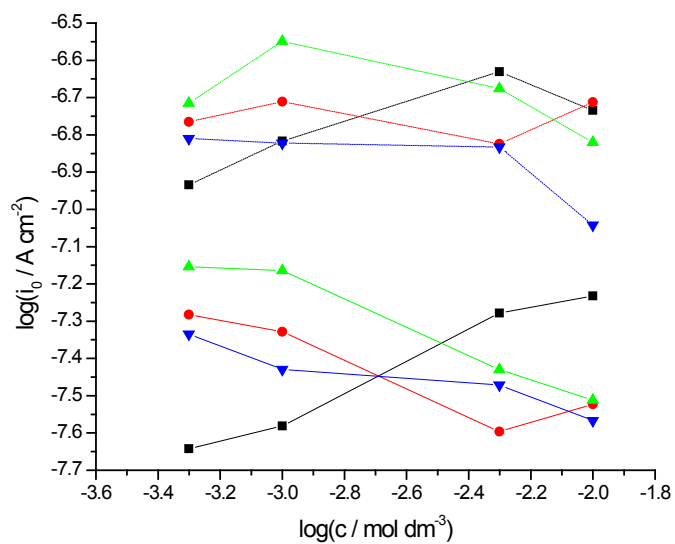
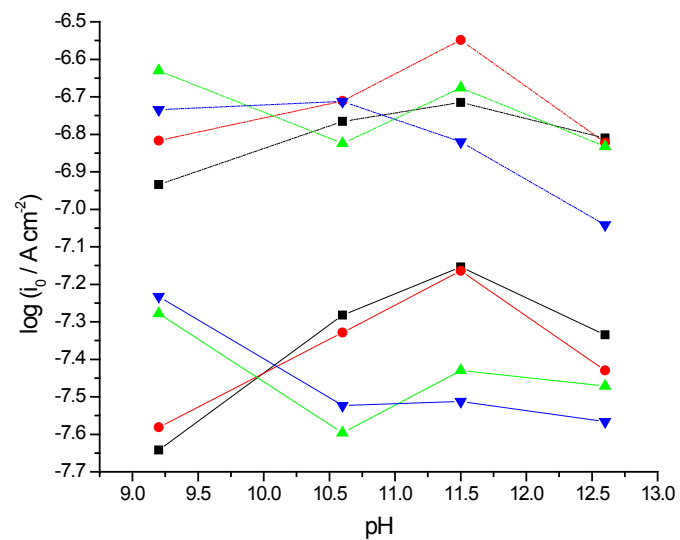


Figure 10: